Check for updates

Macromolecular Materials and Engineering

Macromolecular Materials and Engineering Open Access

www.mame-journal.de

RESEARCH ARTICLE OPEN ACCESS

Smart Graphene-Integrated PCL/COC Ternary Nanocomposites for Enhanced Mechanical Strength and Antibacterial Functionality

Zakia Riaz[1] | Israr Ud Din[1,2] | Kamran A. Khan[1,3]

[1]Department of Aerospace Engineering, Khalifa University of Science and Technology, Abu Dhabi, UAE | [2]Brunel Composite Center, Cambridge, UK | [3]Advanced Research and Innovation Center, Khalifa University of Science and Technology, Abu Dhabi, UAE

Correspondence: Kamran A. Khan (kamran.khan@ku.ac.ae)

Received: 17 January 2026 | **Revised:** 19 August 2026 | **Accepted:** 16 September 2026

Keywords: antibacterial activity | graphene nanoplatelets | PCL/COC nanocomposite | shape memory polymer | thermal stability

ABSTRACT

The development of multifunctional polymeric nanocomposites possessing high mechanical strength, thermal stability, and broad-spectrum antibacterial activity is of significant interest for advanced biomedical and soft robotic applications. In this study, smart PCL/COC/GNP ternary nanocomposites were prepared via a facile and scalable solution-casting method. Incorporation of 10 wt.% COC (cyclic olefin copolymer) into PCL poly(ε-caprolactone) imparted enhanced stiffness and dimensional stability, while graphene nanoplatelets (0.5 and 1.0 wt.%) introduced hierarchical reinforcement and antibacterial functionality. Dynamic mechanical analysis revealed a substantial increase in storage modulus from ~250 MPa (PCL) to ~380 MPa (PCL/COC/GNP-2) and in loss modulus from ~12 to ~39 MPa, demonstrating improved viscoelastic behavior. Thermogravimetric analysis confirmed enhanced thermal stability with delayed degradation onset. The composites exhibited rapid one-way shape memory recovery and broad-spectrum antibacterial efficacy against both Gram-positive *Staphylococcus aureus* and Gram-negative *Escherichia coli*, highlighting their potential as mechanically robust, thermally stable, and antimicrobial smart materials for next-generation biomedical and adaptive structural systems.

1 | Introduction

The growing demand for multifunctional polymeric materials that simultaneously exhibit high mechanical strength, thermal stability, and antibacterial functionality has intensified research into next-generation smart materials [1, 2]. Such systems are particularly crucial for biomedical implants, soft robotic actuators, aerospace morphing structures, and flexible electronics, where adaptability and long-term reliability are equally essential [3–5]. Among these, shape memory polymers (SMPs) have attracted substantial attention due to their ability to recover a predefined shape upon exposure to an external stimulus, typically heat [6]. Their low density, high flexibility, and facile processability, coupled with tunable transition behavior, make them highly suitable for adaptive and reconfigurable applications [7].

Within the family of SMPs, poly(ε-caprolactone) (PCL) has been widely investigated because of its biodegradability, biocompatibility, and low activation temperature (~60°C), which render it ideal for biomedical and temperature-sensitive environments [8–10]. However, neat PCL suffers from low stiffness, limited tensile strength, and weak shape recovery force, which restrict its use in mechanically demanding or repetitive actuation applications [7, 11, 12]. To overcome these shortcomings, polymer blending and nanofiller incorporation have been extensively explored to enhance stiffness, toughness, and functional performance without compromising the shape memory response [13–15].

This is an open access article under the terms of the Creative Commons Attribution License, which permits use, distribution and reproduction in any medium, provided the original work is properly cited.

© 2026 The Author(s). *Macromolecular Materials and Engineering* published by Wiley-VCH GmbH

Cyclic olefin copolymer (COC) has proven to be an effective blending partner for PCL due to its high rigidity, elevated glass transition temperature, and excellent dimensional stability, which together enhance the structural and thermal performance of PCL-based systems [16, 17]. Nevertheless, PCL/COC blending alone may not provide the nanoscale reinforcement and functional characteristics required for multifunctional applications. The incorporation of carbon-based nanofillers therefore offers a rational strategy to further reinforce the PCL/COC framework while introducing additional functionalities [18, 19]. Previous studies have demonstrated the potential of carbon nanomaterials for enhancing PCL performance. Rosehip-derived carbon quantum dots (CQDs) improved the mechanical and biodegradation behavior of PCL films, while CQDs and reduced graphene oxide (RGO) enhanced the mechanical, thermal, and bioactive properties of electrospun PCL nanofibers [20, 21]. Rosehip-derived CQDs also improved the biotribological performance of PCL by reducing friction and wear [22]. In parallel, graphene nanoplatelets (GNPs) have emerged as efficient nanofillers owing to their superior mechanical strength, high thermal conductivity, and inherent antibacterial activity [23–26]. The integration of GNPs promotes interfacial stress transfer, enhanced thermal dissipation, and microbial inhibition through both physical and oxidative mechanisms, offering a pathway toward multifunctional polymer composites [27–30]. However, despite these advances, the synergistic effects of combining COC and GNPs within a PCL-based shape-memory system have not been sufficiently explored, particularly for the simultaneous enhancement of thermomechanical and antibacterial performance. In contrast, the present study develops a ternary PCL/COC/GNP system, where COC strengthens the PCL-based polymeric framework, and GNPs provide additional nanoscale reinforcement and antibacterial functionality. This synergistic design enables combined thermomechanical, shape-memory, and antibacterial performance beyond that of previously reported PCL/carbon-nanofiller systems.

Accordingly, a multifunctional PCL/COC/GNP hybrid shape memory composite system, as illustrated in Figure 1A, was fabricated via a facile and scalable solution-casting method. A constant 10 wt.% of COC was incorporated to improve stiffness and thermal dimensional stability, while GNPs were introduced at 0.5 and 1.0 wt.% to achieve hierarchical reinforcement and antibacterial functionality. Structural and morphological analyses (SEM, EDX, FTIR, and XRD) confirmed homogeneous GNP dispersion and strong interfacial interactions between the polymer phases. Thermogravimetric analysis (TGA) revealed a significant enhancement in thermal stability, with delayed onset of degradation relative to neat PCL and PCL/COC blends. Moreover, antibacterial studies demonstrated that the prepared composites exhibited strong inhibitory effects against both Gram-positive *Staphylococcus aureus* and Gram-negative *Escherichia coli*, confirming their dual-spectrum antibacterial performance (Figure 1B). The synergistic integration of COC and GNPs thus endowed the PCL/COC/GNP composites with exceptional thermomechanical robustness, shape memory efficiency, and antibacterial capability, positioning them as promising candidates for biomedical, soft robotic, and adaptive structural applications.

2 | Materials and Methods

2.1 | Preparation of PCL/COC/GNP Composite Films

Polycaprolactone (PCL, Mw ~80,000, Sigma–Aldrich), Cyclic olefin copolymer (COC, TOPAS 6013), and graphene nanoplatelets (GNPs, XG Sciences) were selected as the base materials. Chloroform (analytical grade) was used as the solvent. Ethyl cellulose (5 wt.% relative to GNP content) was added as a dispersing agent to stabilize GNPs during processing.

PCL and COC were dissolved in chloroform to prepare a 90:10 wt.% polymer blend. A COC content of 10 wt.% was selected based on preliminary screening, providing homogeneous films with suitable rigidity, flexibility, and shape programmability. Separately, GNPs were dispersed in chloroform containing ethyl cellulose and ultrasonicated for 1 h. The GNP dispersion was then added to the PCL/COC solution to achieve filler loadings of 0.5 and 1.0 wt.%. The final mixtures were magnetically stirred for 4 h and cast into 90 mm diameter glass Petri dishes. Films were air-dried for 48 h and vacuum-dried at 40°C for 24 h. Post-drying, the films were annealed at 60°C to enhance structural homogeneity and crystalline alignment. Hereafter, the composites containing 0.5 and 1.0 wt.% GNP are designated as PCL/COC/GNP-1 and PCL/COC/GNP-2, respectively.

2.2 | Morphological and Structural Characterizations

2.2.1 | Scanning Electron Microscopy (SEM) and Energy Dispersive X-Ray Spectroscopy (EDX)

Fractured and surface morphologies of the films were investigated using a JEOL JSM-7610F FE-SEM. Samples were cryo-fractured in liquid nitrogen and sputter-coated with a ~10 nm gold layer to minimize charging. Elemental composition and filler distribution were analyzed using an integrated EDX detector operating at 15 kV.

2.2.2 | Fourier Transform Infrared Spectroscopy (FTIR)

FTIR analysis was conducted on a Bruker Tensor II spectrometer in ATR mode to examine chemical interactions and bonding. Spectra were recorded in the range of 4000–400 cm^{-1} with 4 cm^{-1} resolution at ambient conditions.

2.2.3 | X-Ray Diffraction (XRD)

XRD measurements were carried out using a Bruker D8 Advance diffractometer (Cu Kα, λ = 1.5418 Å). Diffraction data were collected over a 2θ range of 5°–60° at a scanning rate of 2°/min under 40 kV and 30 mA. The crystallinity and possible changes in lattice structures were examined.

14392054, 2026, 9, Downloaded from https://onlinelibrary.wiley.com/doi/10.1002/mame.70360 by NICE, National Institute for Health and Care Excellence, Wiley Online Library on [08/11/2026]. See the Terms and Conditions (https://onlinelibrary.wiley.com/terms-and-conditions) on Wiley Online Library for rules of use; OA articles are governed by the applicable Creative Commons License

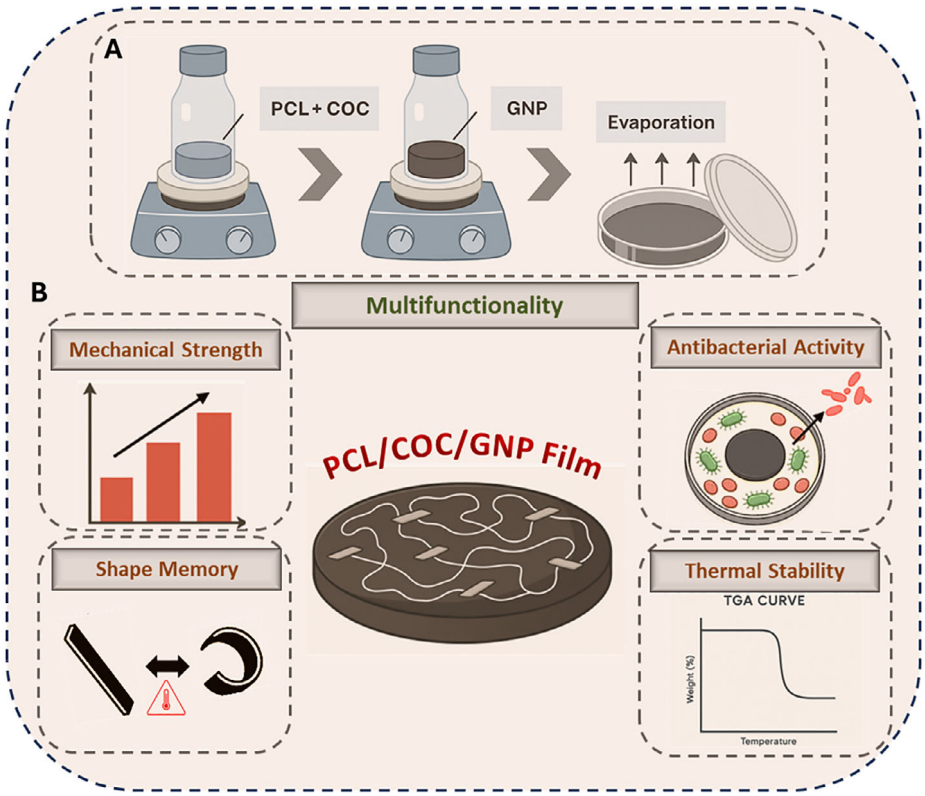


FIGURE 1 | (A) Fabrication route of the PCL/COC/GNP composite film via solution casting. (B) Multifunctional performance showing GNP-enhanced mechanical strength, shape memory, thermal stability, and antibacterial activity.

2.3 | Thermomechanical Characterization

Thermomechanical characterization was carried out using a TA Instruments Q800 dynamic mechanical analyzer (DMA) operated in tensile mode. Rectangular (Gauge length up to 18 mm, width up to 6 mm, thickness ~0.5 mm) were subjected to a temperature sweep from ambient temperature (25C) to 70°C at a heating rate of 3°C min^{-1} with a fixed frequency of 1 Hz. The variations in storage modulus (E′) and loss modulus (E″) were recorded to evaluate the thermal mechanical behavior of the samples. Frequency sweep measurements were additionally performed over 10–80 Hz at a fixed temperature and within the linear viscoelastic region to evaluate the frequency-dependent viscoelastic response. Shape memory performance was further examined by deforming the specimens at 65°C, fixing the temporary shape upon cooling, and monitoring the recovery during subsequent reheating.

2.4 | Shape Memory Demonstration

To evaluate the shape memory behavior and actuation capability of the prepared composites, ribbon-shaped specimens (40 mm × 10 mm × 1 mm) were heated above their transition temperature and manually deformed into a U-shaped configuration (~180° bend). The deformed samples were secured using metallic clips and cooled to ambient temperature to fix the temporary shape. Upon cooling, the clips were removed, and the specimens successfully retained their deformed configuration, confirming efficient shape fixation. When reheated above the transition temperature, the ribbons gradually and completely recovered their original flat geometry, demonstrating a distinct and reversible shape memory effect. Sequential photographs were captured to visually report the deformation and recovery processes. Furthermore, to highlight the material's versatility, the PCL/COC/GNP composite films were deformed into a flower-like structure at elevated temperature and subsequently immersed in a hot water bath, exhibiting time-dependent recovery to their original flat morphology, thereby confirming their responsive and programmable shape memory behavior.

2.5 | Thermogravimetric Analysis

Thermogravimetric analysis (TGA) was carried out using a TA Instruments SDT Q600 system to study the thermal behavior and weight loss profile of the samples upon heating. Approximately 13–15 mg of each sample was placed in an alumina crucible and heated from room temperature to 500°C at a constant rate of 5°C min^{-1} under an inert nitrogen environment. The resulting TGA curves were used to evaluate the weight loss pattern to know about thermal stability of the materials.

2.6 | Bacterial Culture and Antibacterial Activity Test

The antibacterial efficiency of the PCL/COC/GNP-1 and PCL/COC/GNP-2 composite films was evaluated against *Escherichia coli* (Gram-negative) and *Staphylococcus aureus*

14392054, 2026, 9, Downloaded from https://onlinelibrary.wiley.com/doi/10.1002/mame.70360 by NICE, National Institute for Health and Care Excellence, Wiley Online Library on [08/11/2026]. See the Terms and Conditions (https://onlinelibrary.wiley.com/terms-and-conditions) on Wiley Online Library for rules of use; OA articles are governed by the applicable Creative Commons License

(Gram-positive) using the disc diffusion and time-dependent growth inhibition methods. Bacterial cultures were freshly prepared in nutrient broth and incubated at 37°C for 24 h to obtain actively growing cells. After incubation, 100 µL of each bacterial suspension was uniformly spread onto sterile nutrient agar plates. Pre-cut and sterilized film samples were carefully placed on the agar surface, and the plates were incubated again at 37°C for 24 h. The antibacterial response of the composites was determined by measuring the diameter of the inhibition zones formed around the samples. Ciprofloxacin discs were used as the reference antibacterial standard. Each experiment was conducted in triplicate to ensure reproducibility.

For the dynamic antibacterial test, pre-sterilized film pieces were placed at the bottom of 24-well culture plates. One milliliter of bacterial suspension was added to each well, and the plates were maintained at 37°C on an orbital shaker operating at approximately 90 rpm. Optical density (OD_{600}) readings were recorded at selected time intervals of 5, 10, 15, and 20 h using a Synergy H1 multimode microplate reader (BioTek) to monitor bacterial growth in the presence of the nanocomposite films. The progressive decline in OD values was used as an indicator of bacterial growth suppression over time.

To investigate morphological changes in bacterial cells after contact with the films, scanning electron microscopy (SEM) analysis was carried out. Bacterial suspensions were placed on clean silicon wafers and fixed with 2% glutaraldehyde solution for approximately 3 h at ambient temperature. The fixed samples were dehydrated using graded ethanol solutions (50%, 70%, 90%, and 100%), followed by drying with liquid nitrogen to preserve cell structure. The dried specimens were coated with a thin layer of gold and imaged under SEM to visualize the structural alterations caused by interaction with the PCL/COC/GNP composites.

3 | Results and Discussion

3.1 | Structural Analysis

Fourier transform infrared (FTIR) spectroscopy was employed to examine molecular interactions among PCL, COC, and GNP components in the composite films as shown in Figure 2A. The pristine PCL spectrum displayed characteristic absorption bands at 2942 and 2865 cm^{-1} corresponding to asymmetric and symmetric —CH_2– stretching vibrations, while a prominent peak at 1720 cm^{-1} was ascribed to the C═O stretching of ester groups. The absorption at 1293 and 1240 cm^{-1} related to the —C—O and —O—C— stretching vibrations of the aliphatic ester backbone further confirmed the semi-crystalline nature of PCL [31]. In contrast, pure COC revealed relatively weaker signals, with subtle bands near 2925 and 2854 cm^{-1} (—CH stretching) and a broad shoulder around 1470–1450 cm^{-1}, indicating the presence of alicyclic rings typical of its amorphous character [16]. Detailed FTIR analysis revealed subtle changes in characteristic PCL bands upon COC blending and GNP incorporation. The C—H stretching band shifted from 2943 cm^{-1} in neat PCL to 2944 cm^{-1} in PCL/COC, indicating changes in chain packing associated with weak non-covalent PCL–COC interactions. Upon GNP addition, this band further shifted to 2946 cm^{-1}, suggesting additional polymer–GNP interfacial interactions. The PCL-associated band at 1162 cm^{-1} shifted to 1160 cm^{-1} in the blend and returned to 1162 cm^{-1} in the hybrid. In contrast, the PCL carbonyl band remained unchanged at 1721 cm^{-1} in all systems. These subtle shifts, together with the absence of new bands, support predominantly physical/non-covalent interactions and local chain rearrangement rather than new covalent bond formation [32].

To complement the molecular findings, x-ray diffraction (XRD) patterns were recorded to investigate crystalline features and structural rearrangement upon blending and filler integration (Figure 2B). Pure PCL exhibited distinct diffraction peaks at $2\theta = 21.4°$ and 23.8°, corresponding to the (110) and (200) planes of its orthorhombic crystalline phase [33]. These reflections confirm the semi-crystalline character of PCL, consistent with literature-reported values. The XRD pattern of pure COC, in contrast, showed a diffuse halo centered around $2\theta \approx 14°–20°$, characteristic of its amorphous morphology [34]. In the PCL/COC 90:10 blend, a slight reduction in peak intensity and marginal peak broadening were observed, indicating a decrease in overall crystallinity due to disruption of PCL lamellar packing by the amorphous COC domains. Upon incorporation of GNPs, the PCL diffraction peaks were retained but slightly shifted and further broadened, particularly at higher GNP concentrations, suggesting lattice distortion and constrained crystallite growth. Notably, no distinct peaks corresponding to graphitic planes of GNP (typically near $2\theta \approx 26.5°$ for (002) were observed. The weak/undetectable GNP reflection is mainly associated with the low GNP loading and its relatively weak diffraction contribution within the polymer matrix. Furthermore, the absence or reduction of a nanofiller diffraction peak alone cannot conclusively establish the extent of exfoliation [35].

Quantitative analysis using the XRD integrated peak-area method yielded crystallinity (Xc) values of 38.54%, 30.53%, and 36.37% for PCL, PCL/COC, and PCL/COC/GNP, respectively. The decrease in (Xc) upon COC incorporation reflects the contribution of its amorphous phase, whereas the subsequent increase with GNP incorporation suggests enhanced crystalline organization within the PCL/COC matrix.

3.2 | Morphological Analysis

The surface and cross-sectional morphology of the prepared films was analyzed using field emission scanning electron microscopy (SEM) to gain insights into the dispersion of fillers, interfacial compatibility, and structural uniformity. The neat PCL film exhibited a relatively rough surface with micro-scale irregularities and no defined features, indicative of its semicrystalline morphology [36, 37]. In contrast, the pure COC film showed a homogeneously smooth texture, consistent with its amorphous structure [16]. Upon blending 10 wt.% COC into the PCL matrix, a notable morphological transition was observed; the surface displayed subtle phase interlocking and finer textures, reflecting enhanced interfacial compatibility and partial miscibility between the two polymers (Figure 2C). The introduction of graphene nanoplatelets (GNPs) led to a more rugged and textured surface morphology across all hybrid films. The SEM micrographs of PCL/COC/GNP reveal platelet-like GNP-associated features distributed throughout the polymer matrix, with no prominent large-scale agglomerates observed at the investigated

14392054, 2026, 3, Downloaded from https://onlinelibrary.wiley.com/doi/10.1002/mame.70360 by NICE, National Institute for Health and Care Excellence, Wiley Online Library on [08/11/2026]. See the Terms and Conditions (https://onlinelibrary.wiley.com/terms-and-conditions) on Wiley Online Library for rules of use; OA articles are governed by the applicable Creative Commons License

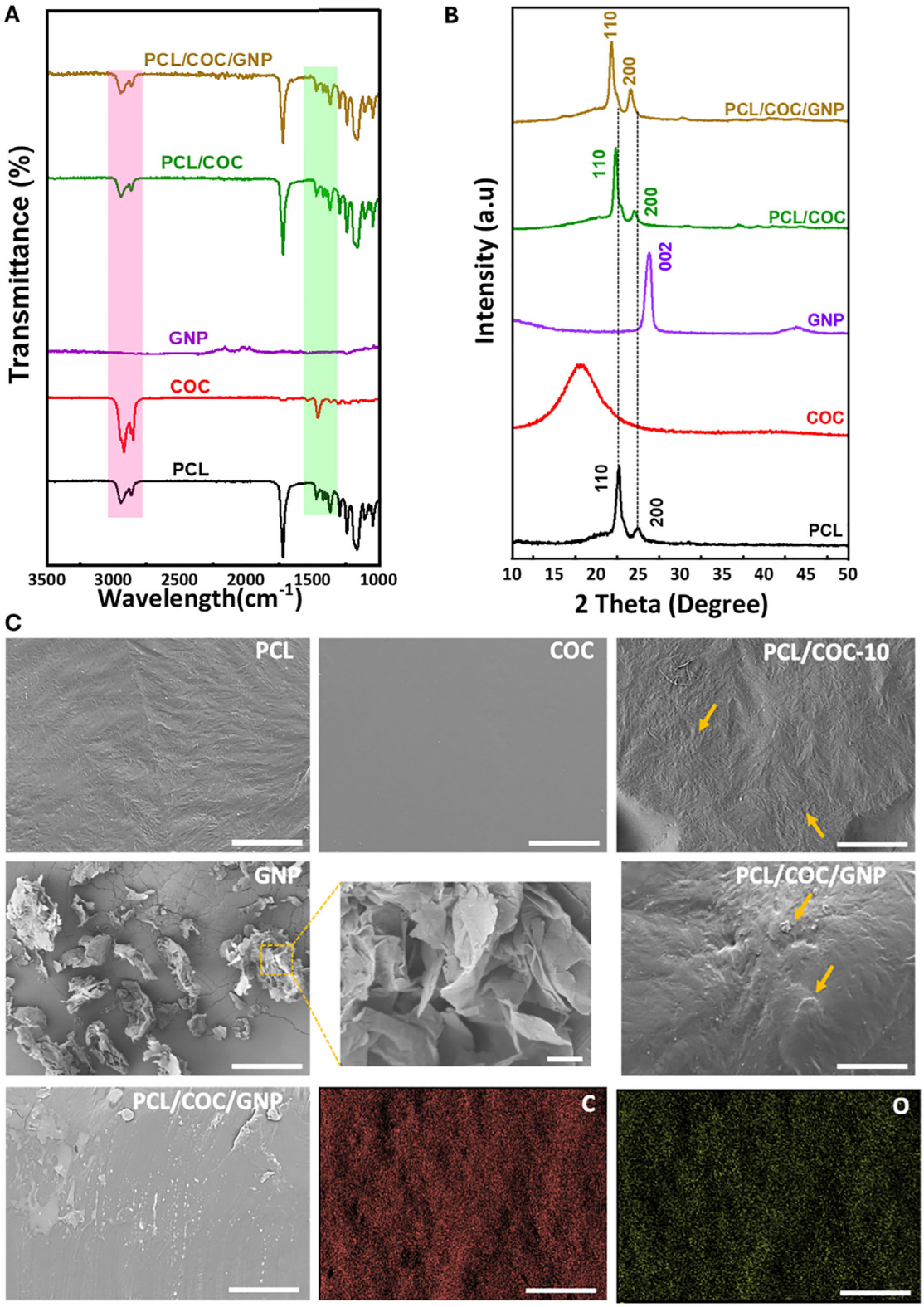


FIGURE 2 | Comprehensive structural and morphological characterization of PCL, COC, GNP, and PCL/COC/GNP hybrid composites. (A) FTIR spectra identifying characteristic functional groups and confirming molecular interactions among the components. (B) XRD patterns revealing the semi-crystalline nature of PCL and the presence of GNPs, with peak shifts indicating improved filler–matrix compatibility. (C) SEM images displaying surface morphologies and dispersion states (scale bar = 10 and 1 μm), with EDX elemental mapping confirming uniform carbon and oxygen distribution in the hybrid matrix.

14392054, 2026, 9, Downloaded from https://onlinelibrary.wiley.com/doi/10.1002/mame.70360 by NICE, National Institute for Health and Care Excellence, Wiley Online Library on [08/11/2026]. See the Terms and Conditions (https://onlinelibrary.wiley.com/terms-and-conditions) on Wiley Online Library for rules of use; OA articles are governed by the applicable Creative Commons License

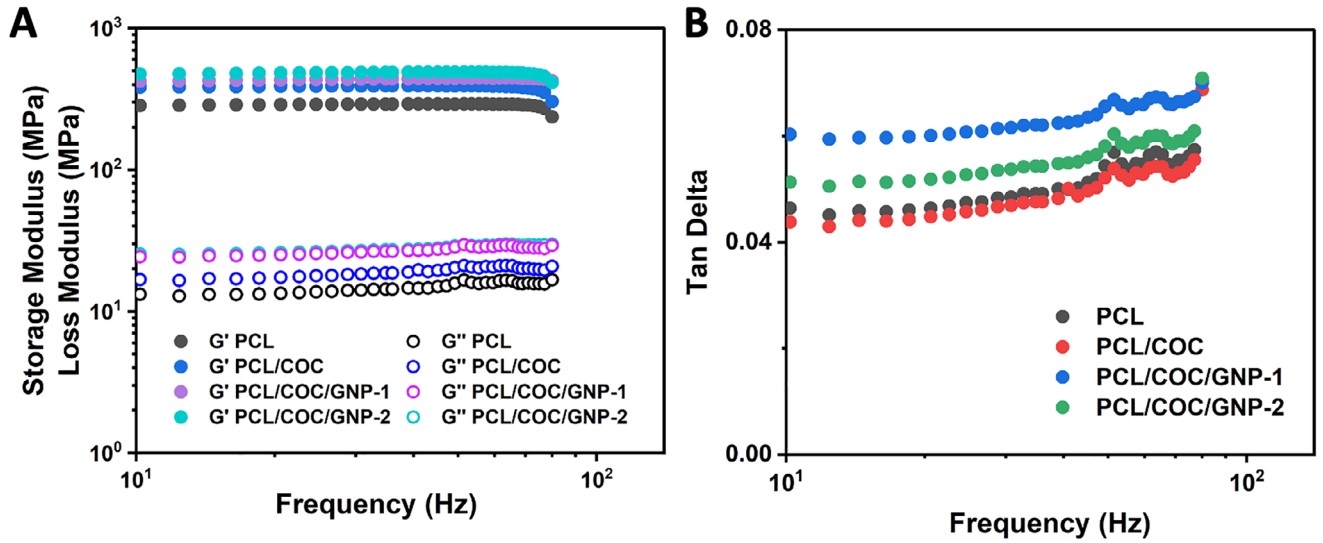


FIGURE 3 | Frequency-sweep analysis showing (A) storage and loss moduli and (B) tan δ of PCL, PCL/COC, and PCL/COC/GNP composites.

scale. The relatively homogeneous distribution suggests that GNP dispersion was largely maintained during composite preparation, promoting effective interfacial contact with the surrounding polymer phases and potentially contributing to improved stress transfer and overall composite performance [38, 39]. Elemental mapping via energy-dispersive x-ray spectroscopy (EDX) further supported these findings, showing consistent and homogeneous distribution of carbon and oxygen throughout the matrix, confirming the successful incorporation and dispersion of GNPs within the PCL/COC composite framework.

3.3 | Thermomechanical Analysis

Frequency-sweep analysis was performed at 25°C to investigate the viscoelastic response of the PCL, PCL/COC, and hybrid materials under dynamic loading. The storage modulus (E′) remained consistently higher than the loss modulus (E″) throughout the investigated frequency range, indicating predominantly elastic behavior (Figure 3A). Incorporation of COC and GNPs increased both E′ and E″ relative to neat PCL, with the GNP-reinforced composites exhibiting the highest moduli, suggesting enhanced stiffness and restricted polymer-chain mobility. Moreover, the absence of an E′–E″ crossover indicates that the elastic response remained dominant over the tested frequency range. The relatively low tan δ values (~0.04–0.07), with only a slight increase with frequency, further indicate limited viscous dissipation and suppressed segmental relaxation, confirming the enhanced dynamic stability of the reinforced composites (Figure 3B). To further elucidate the thermomechanical response, the temperature-dependent evolution of the storage and loss moduli was subsequently investigated.

The temperature-dependent dynamic mechanical response of the neat PCL, PCL/COC blend, and two graphene nanoplatelet (GNP)-reinforced hybrids was investigated through DMA to evaluate their storage modulus (E′) and loss modulus (E″). As shown in Figure 4A, the neat PCL film exhibits a storage modulus of ~250 MPa at 30°C, which progressively declines with temperature and experiences a pronounced drop beyond 55°C, reflecting the transition from the glassy to rubbery phase. Upon incorporation of COC, the PCL/COC blend displays a moderately elevated initial E′ of ~290 MPa, with the transition shifted toward higher temperatures, indicating enhanced chain rigidity and suppressed segmental mobility. Further addition of GNPs in the hybrid systems leads to a notable reinforcement effect. The PCL/COC/GNP-1 system demonstrates an E′ of ~350 MPa, while PCL/COC/GNP-2 shows a maximum value of ~380 MPa, sustaining higher stiffness across the temperature range and suggesting efficient load transfer between the matrix and nanoplatelets. This progressive improvement in modulus from neat to hybrid systems confirms the synergistic contribution of both COC and GNPs in enhancing thermomechanical robustness.

The evolution of the loss modulus (E″) with temperature offers insight into the dissipation behavior and α-transition of the systems (Figure 4B). The neat PCL shows a peak E″ of ~12.5 MPa centered around 55°C, associated with the relaxation of the amorphous phase. In the blend, the E″ peak increases to ~20 MPa and shifts to 58°C, reflecting restricted chain dynamics due to the miscibility and segmental interaction with COC. For the PCL/COC/GNP-1 system, a substantial rise in E″ to ~28 MPa is observed at 60°C, and the PCL/COC/GNP-2 system peaks at ~39 MPa near 62°C, indicative of increased energy dissipation and internal friction induced by GNP incorporation. The results reveal that the hybrid systems, particularly PCL/COC/GNP-2, exhibit superior thermomechanical performance; hence, this composition was further utilized for shape memory evaluation and compared with the PCL/COC blend and neat PCL to examine the effect of graphene nanoplatelet incorporation.

3.4 | Shape Memory Response

The shape memory characteristics of the PCL/COC/GNP-2 hybrid composites were systematically investigated through thermomechanical programming and actuation demonstrations. The shape memory cycle involves deformation above the transition temperature, followed by cooling to fix the temporary configuration, and reheating to recover the original geometry, driven

14392054, 2026, 9, Downloaded from https://onlinelibrary.wiley.com/doi/10.1002/mame.70360 by NICE, National Institute for Health and Care Excellence, Wiley Online Library on [08/11/2026]. See the Terms and Conditions (https://onlinelibrary.wiley.com/terms-and-conditions) on Wiley Online Library for rules of use; OA articles are governed by the applicable Creative Commons License

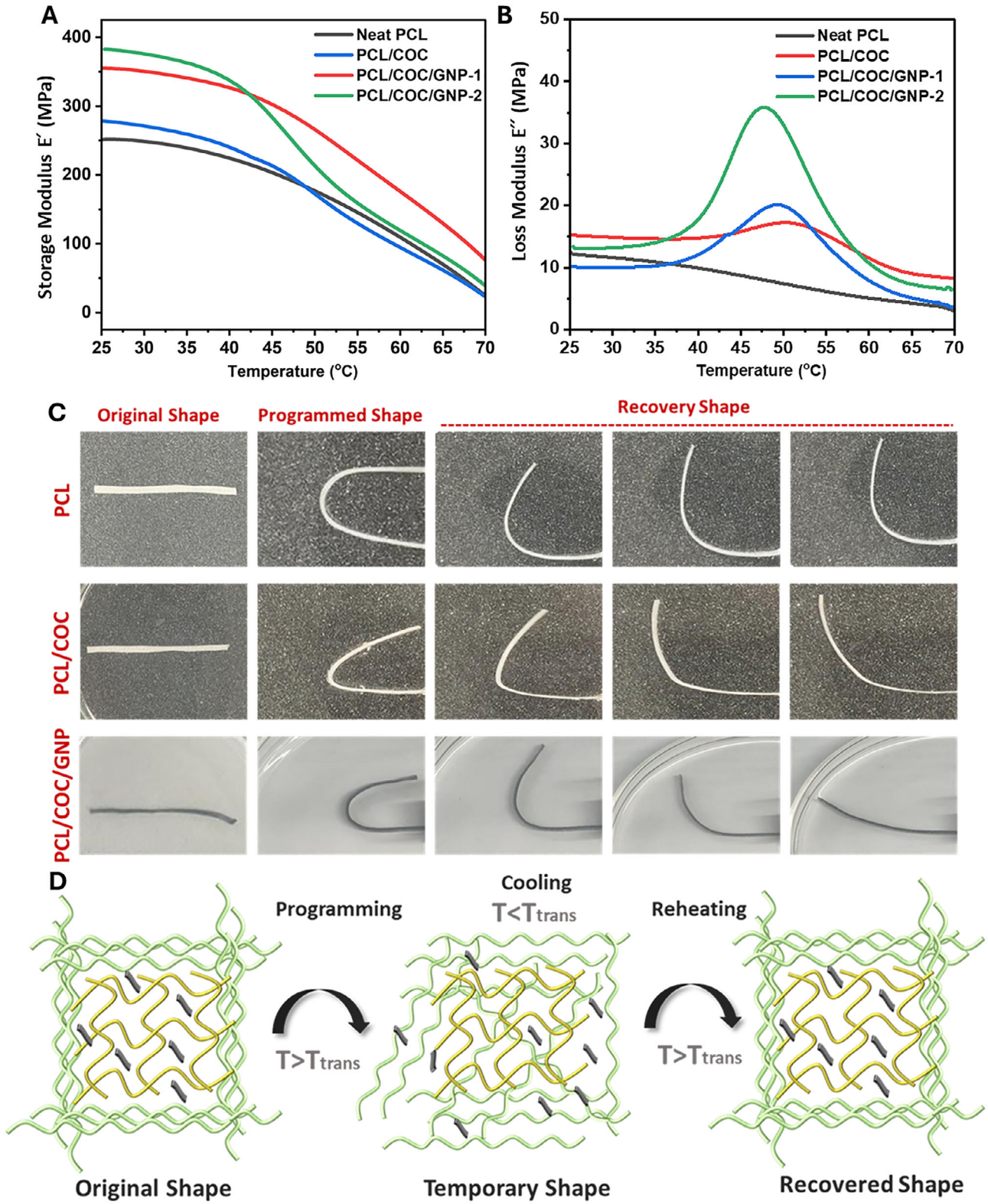


FIGURE 4 | Dynamic mechanical analysis and visual demonstration of the shape memory behavior of neat PCL, PCL/COC, and PCL/COC/GNP composites. (A) Storage modulus (E′) and (B) Loss modulus (E″) variation with temperature. (C) Sequential images illustrating the original, programmed, and recovered shapes of the samples, demonstrating efficient shape fixation and recovery. (D) Schematic representation of the molecular mechanism of shape memory, depicting polymer chain rearrangement during programming, cooling, and reheating cycles.

14392054, 2026, 9, Downloaded from https://onlinelibrary.wiley.com/doi/10.1002/mame.70360 by NICE, National Institute for Health and Care Excellence, Wiley Online Library on [08/11/2026]. See the Terms and Conditions (https://onlinelibrary.wiley.com/terms-and-conditions) on Wiley Online Library for rules of use; OA articles are governed by the applicable Creative Commons License

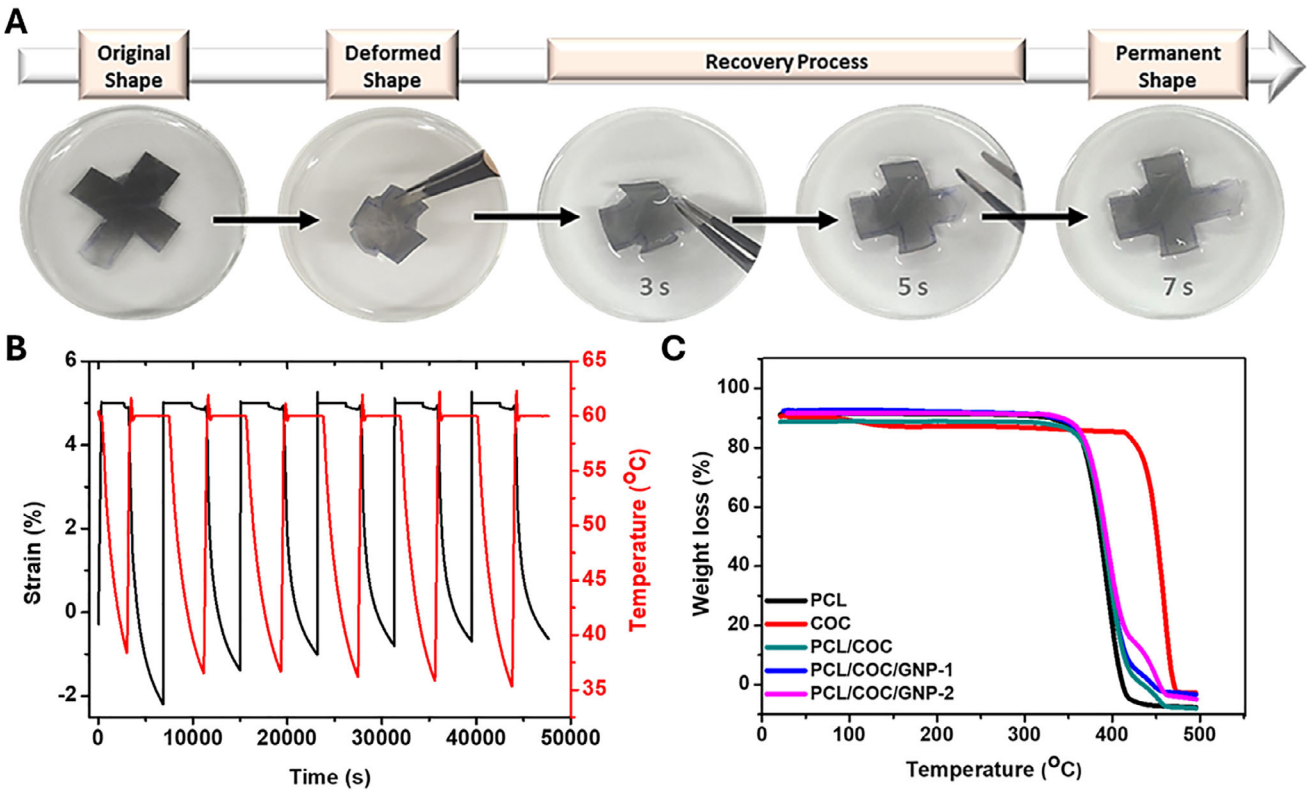


FIGURE 5 | (A) One-way shape memory (SMP) cycle of the flower-shaped PCL/COC/GNP composite film showing deformation, fixation, and recovery to its permanent shape. (B) Cyclic shape memory behavior of the PCL/COC/GNP-2 composite during repeated programming and recovery cycles. (C) TGA curves of neat PCL, PCL/COC, and PCL/COC/GNP composites indicating enhanced thermal stability with GNP incorporation.

by entropy release in the polymer network [40]. Comparative analysis in Figure 4C highlights the enhanced recovery behavior of the ternary hybrid over pristine PCL and the PCL/COC blend. While the neat PCL sample exhibits partial recovery due to limited elasticity and low modulus, the addition of COC improves shape fixity but does not eliminate residual deformation. In contrast, the PCL/COC/GNP composite achieves nearly complete recovery with reduced residual strain, attributed to improved thermal conductivity, nanoparticle-induced reinforcement, and enhanced interfacial adhesion. The chain reconfiguration process underlying these observations is depicted schematically in Figure 4D, showing reversible molecular alignment and relaxation across thermal cycles. The practical applicability of the composite system is demonstrated in Figure 5A provides a time-resolved view of shape recovery in an *X*-type flower-shaped actuator at 3, 5, and 7 s, illustrating the rapid and progressive restoration of the original configuration with high shape fidelity.

The strain-controlled shape memory cyclic tests were performed to investigate the one-way shape memory behavior of the PCL/COC/GNP-2.

Composite, as shown in Figure 5B. Above its transition temperature (Tg), the material exhibits a rubbery-elastic state that allows deformation and storage of the temporary shape, while below Tg it becomes rigid, enabling the fixed shape to be maintained. The sample was pre-heated to 60°C, above the Tg, and equilibrated for 10 min before applying a uniaxial strain of 5%. The specimen was then cooled to 35°C at a rate of 0.4°C min^{-1} while maintaining the applied strain, resulting in effective shape fixation. After cooling, the external load was released, and a fixed strain ≈ 4.75% was retained, corresponding to a shape fixity ratio ≈ 95%. Upon reheating to 60°C, the polymer rapidly recovered its original shape. The overlapping strain–temperature curves across multiple cycles confirmed the good reversibility, stability, and repeatability of the one-way shape memory performance of the PCL/COC/GNP-2 composite.

3.5 | Thermal Stability

The thermogravimetric analysis (TGA) of PCL, COC, PCL/COC, PCL/COC/GNP-1, and PCL/COC/GNP-2 composites over the temperature range of 20°C to 500°C revealed distinct variations in their thermal degradation behavior (Figure 5C). Pure PCL exhibited the lowest thermal stability, with the onset of decomposition occurring around 320°C, while pure COC began to degrade at approximately 370°C, indicating higher thermal resistance. The PCL/COC blend showed an intermediate degradation onset near 350°C, suggesting improved stability due to the incorporation of COC. The addition of graphene nanoplatelets (GNPs) further enhanced the thermal performance of the composites. PCL/COC/GNP-1 started degrading at around 380°C, whereas PCL/COC/GNP-2 displayed the greatest thermal stability, with decomposition initiating near 400°C and extending beyond 450°C. The improved thermal resistance of the nanocomposites is attributed to the barrier effect and strong interfacial interactions between the GNPs and the polymer matrix, which hinder the

14392054, 2026, 9, Downloaded from https://onlinelibrary.wiley.com/doi/10.1002/mame.70360 by NICE, National Institute for Health and Care Excellence, Wiley Online Library on [08/11/2026]. See the Terms and Conditions (https://onlinelibrary.wiley.com/terms-and-conditions) on Wiley Online Library for rules of use; OA articles are governed by the applicable Creative Commons License

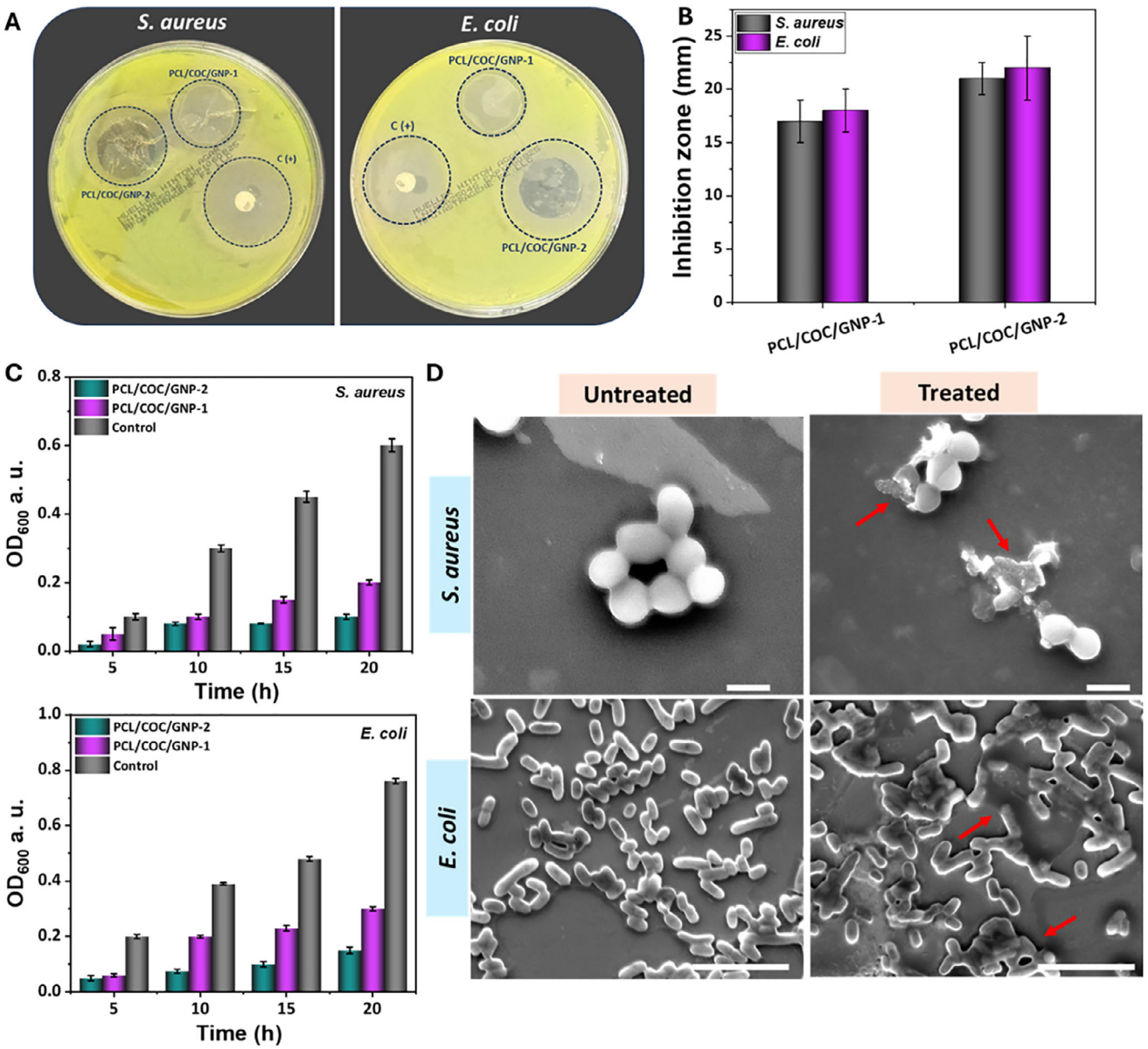


FIGURE 6 | Antibacterial activity and interaction mechanism of PCL/COC/GNP composites against *S. aureus* and *E. coli*. (A) Zone of inhibition assay demonstrating antibacterial efficacy of PCL/COC/GNP-1 and PCL/COC/GNP-2 composites. (B) Quantitative measurement of the diameter of the inhibition zones for *S. aureus* and *E. coli*. (C) Time-dependent antibacterial activity of the composites against both bacterial strains. (D) SEM images of *S. aureus* (scale bar = 1 μm) and *E. coli* (scale bar = 5 μm) before and after 5 h contact with the composite films; red arrows indicate bacterial cell death.

diffusion of degradation products and restrict polymer chain mobility. At 500°C, the residual masses were approximately 1.28% for PCL, 6.69% for COC, 4.42% for PCL/COC, 3.1% for PCL/COC/GNP-1, and 3.3% for PCL/COC/GNP-2. Although GNP incorporation did not increase the final residual mass relative to the PCL/COC blend, the delayed degradation observed for the GNP-containing composites indicates improved thermal stability, which may be associated with the barrier effect of GNPs in restricting heat and mass transport during decomposition.

3.6 | Antibacterial Activity

The antibacterial activity of the PCL/COC/GNP composite films was investigated against *Staphylococcus aureus* and *Escherichia coli* through the agar diffusion and OD analyses. The agar diffusion test confirmed that both composite films exhibited clear inhibition zones, demonstrating effective antibacterial behavior (Figure 6A). The zone of inhibition for *S. aureus* was 16 mm for PCL/COC/GNP-1 and 21.9 mm for PCL/COC/GNP-2, while for *E. coli* it was 18 and 22.9 mm, respectively (Figure 6B). The increase in inhibition zone diameter with higher GNP loading indicated that the antibacterial activity of the films was directly related to graphene nanoplatelet concentration.

To further investigate the antibacterial properties of the nanocomposite films, 1 mL of bacterial suspension was added into 24-well plates containing the prepared films. The plates were placed on a mechanical shaker at a speed of approximately 90 rpm

14392054, 2026, 9, Downloaded from https://onlinelibrary.wiley.com/doi/10.1002/mame.70360 by NICE, National Institute for Health and Care Excellence, Wiley Online Library on [08/11/2026]. See the Terms and Conditions (https://onlinelibrary.wiley.com/terms-and-conditions) on Wiley Online Library for rules of use; OA articles are governed by the applicable Creative Commons License

and incubated at 37°C for time intervals of 5, 10, 15, and 20 h. Subsequently, the optical density (OD_{600}) of the bacterial suspensions was recorded to evaluate bacterial growth. The OD results obtained were in good agreement with the findings of the agar diffusion method, showing that the bacterial growth decreased progressively with time in the presence of GNP-containing films. The reduction in OD values was more pronounced for PCL/COC/GNP-2, indicating stronger antibacterial activity due to the higher graphene content and better interfacial contact with bacterial cells (Figure 6C).

The enhanced antibacterial performance of the composite films can be attributed to the unique physicochemical characteristics of graphene nanoplatelets. The proposed mechanism involves direct physical interaction between the sharp edges of GNPs and bacterial cell walls, causing membrane disruption, leakage of cytoplasmic contents, and eventual cell death. The large surface area of GNPs further facilitates close contact with bacterial membranes, intensifying these interactions [41–43]. In addition to physical membrane damage, GNPs may induce oxidative stress through the generation of reactive oxygen species (ROS), including superoxide radicals (O_2•), hydroxyl radicals (•OH), and hydrogen peroxide (H_2O_2). These ROS can cause oxidative damage to membrane lipids, proteins, and intracellular components, further compromising bacterial cell integrity. Therefore, the antibacterial activity of PCL/COC/GNP composites likely results from the combined effects of GNP-induced physical membrane disruption and ROS-mediated oxidative stress [44, 45].

Scanning electron microscopy (SEM) further supported these observations, as shown in Figure 6D. Untreated bacterial cells exhibited smooth and intact surfaces, whereas cells exposed to GNP-based composites appeared collapsed, wrinkled, and ruptured, with visible cytoplasmic leakage. These morphological deformations confirm that the antibacterial effect of the PCL/COC/GNP films arises mainly from mechanical disruption and membrane lysis induced by the sharp-edged graphene nanoplatelets embedded in the polymer matrix.

4 | Conclusion

In summary, multifunctional PCL/COC/GNP ternary nanocomposites were successfully fabricated via a facile solution-casting approach, exhibiting remarkable improvements in mechanical, thermal, and antibacterial performance. The synergistic incorporation of COC and graphene nanoplatelets resulted in strong interfacial interactions, enhanced stiffness, and superior viscoelastic behavior, as evidenced by the significant increase in storage and loss moduli. Thermogravimetric analysis confirmed improved thermal stability with delayed degradation onset, while shape memory studies demonstrated rapid and reversible actuation with high recovery precision. Furthermore, the composites exhibited broad-spectrum antibacterial activity against both *Staphylococcus aureus* and *Escherichia coli*, validating their dual functional performance. These findings establish the developed PCL/COC/GNP nanocomposites as promising candidates for next-generation biomedical devices, soft robotics, and adaptive structural applications.

Author Contributions

Zakia Riaz: conceptualization, methodology, investigation, visualization, Writing – review and editing, Writing – original draft. **Israr Ud Din**: software, writing – review and editing. **Kamran A. Khan**: conceptualization, project administration, resources, supervision, funding acquisition.

Acknowledgements

This publication is based on work supported by Khalifa University of Science and Technology under Award No. CIRA-2021-054

Conflicts of Interest

The authors declare no conflicts of interest.

Data Availability Statement

The data that support the findings of this study are available from the corresponding author upon reasonable request.

References

1. Z. Riaz, S. Baddi, F. Gao, X. Qiu, and C. Feng, "Supramolecular Polymer Co-Assembled Multifunctional Chiral Hybrid Hydrogels with Adhesive, Self-Healing and Antibacterial Properties," *Gels* 10 (2024): 489, https://doi.org/10.3390/gels10080489.

2. Z. Riaz, S. Baddi, F. Gao, and C. L. Feng, "Gallic Acid-Doped Multifunctional Hybrid Hydrogel for Antioxidant and Antibacterial Studies," *European Polymer Journal* 206 (2024): 112778, https://doi.org/10.1016/J.EURPOLYMJ.2024.112778.

3. L. Luo, F. Zhang, L. Wang, Y. Liu, and J. Leng, "Recent Advances in Shape Memory Polymers: Multifunctional Materials, Multiscale Structures, and Applications," *Advanced Functional Materials* 34 (2024): 2312036, https://doi.org/10.1002/ADFM.202312036.

4. G. Ghosh, R. Bhattacharyya, and D. Penumadu, "Advances in Multi-Functional Composite Materials: Applications and Opportunities in Automotive Industry," *Functional Composites and Structures* 7 (2025): 042001, https://doi.org/10.1088/2631-6331/AE1350.

5. I. A. Rashid and A. Afzal, "Smart Polymers and Composites," *Advanced Functional Polymers: Synthesis to Applications* (Springer, 2023), 77–99, https://doi.org/10.1007/978-981-99-0787-8.

6. X. Zhang, W. Tang, D. Yang, J. Ma, X. Li, and G. Tian, "The Latest Advances in Two-Way Shape Memory Polymers: Fabrication Strategies, Programming Mechanisms, and Emerging Applications," *Chemical Engineering Journal* 521 (2025): 166372, https://doi.org/10.1016/J.CEJ.2025.166372.

7. S. K. Chandaka, A. Das, and P. Laskar, "Emergence of Shape Memory Polymers as a New Material for Diverse Applications," *RSC Advances* 15 (2025): 31210–31229, https://doi.org/10.1039/D5RA04372G.

8. S. Gopinath, N. N. Adarsh, P. R. Nair, and S. Mathew, "Recent Trends in Thermo-Responsive Elastomeric Shape Memory Polymer Nanocomposites," *Polymer Composites* 44 (2023): 4433–4458, https://doi.org/10.1002/PC.27464.

9. R. Sachan, S. G. Warkar, and R. Purwar, "An Overview on Synthesis, Properties and Applications of Polycaprolactone Copolymers, Blends & Composites," *Polymer-Plastics Technology and Materials* 62 (2023): 327–358, https://doi.org/10.1080/25740881.2022.2113890.

10. V. Hada, S. A. R. Hashmi, M. Mili, et al., "Polycaprolactone-Based Shape Memory Polymeric Nanocomposites for Biomedical Applications," *Food, Medical, and Environmental Applications of Nanomaterials* (2022): 413–433, https://doi.org/10.1016/B978-0-12-822858-6.00014-5.

11. K. I. Matumba, T. C. Mokhena, V. Ojijo, E. R. Sadiku, and S. S. Ray, "Morphological Characteristics, Properties, and Applications of Polylactide/Poly(ε-caprolactone) Blends and Their Composites—A

14392054, 2026, 9, Downloaded from https://onlinelibrary.wiley.com/doi/10.1002/mame.70360 by NICE, National Institute for Health and Care Excellence, Wiley Online Library on [08/11/2026]. See the Terms and Conditions (https://onlinelibrary.wiley.com/terms-and-conditions) on Wiley Online Library for rules of use; OA articles are governed by the applicable Creative Commons License

Review," *Macromolecular Materials and Engineering* 309 (2024): 2400056, https://doi.org/10.1002/MAME.202400056.

12. M. Ngwenya, T. P. Gumede, R. Arpad, P. Camargo, and B. Motloung, "Nanocellulose-Reinforced Poly(Lactic Acid) and Poly(ε-caprolactone) Bio-Nanocomposites: a Review and Future Outlook for Poly(Lactic Acid)/Poly(ε-caprolactone) Blend Systems," *Materials* 18 (2025): 5172, https://doi.org/10.3390/MA18225172.

13. M. R. Abdullah, Z. Peng, V. babu Rajendren, et al., "Comprehensive Review of 3D/4D Printing of Soft Materials, Methods and Applications," *Applied Materials Today* 43 (2025): 102667, https://doi.org/10.1016/J.APMT.2025.102667.

14. N. Bisht, J. Vishwakarma, S. Jaiswal, et al., "Synergizing Chemistry: Unveiling the Potential of Hybrid Fillers for Enhanced Performance in Shape Memory Polymers," *Advanced Composites and Hybrid Materials* 8 (2024): 7, https://doi.org/10.1007/S42114-024-01059-2.

15. T. Li, L. Chen, Y. Yuan, and R. Shi, "The Current Status, Prospects, and Challenges of Shape Memory Polymers Application in Bone Tissue Engineering," *Polymers* 15 (2023): 556, https://doi.org/10.3390/POLYM15030556.

16. Z. Riaz, A. N. Khan, S. R. Abbas, and Z. Hussain, "Structure-Properties Relationships of Novel Cyclic Olefinic Copolymer/Poly(L-Lactic acid) Polymer Blends," *Journal of Materials Research and Technology* 9 (2020): 7172–7179, https://doi.org/10.1016/J.JMRT.2020.05.024.

17. Z. Riaz, M. Ali, A. D. Abbasi, K. A. Khan, and O. Aydin, "Multifunctional Cyclic Olefin Copolymer-Titanium Dioxide-Based Nanocomposites for Enhanced Antibacterial and Biocompatible Properties," *ACS Omega* 10 (2025): 15052–15064, https://doi.org/10.1021/ACSOMEGA.4C10536.

18. C. Cha, S. R. Shin, N. Annabi, M. R. Dokmeci, and A. Khademhosseini, "Carbon-Based Nanomaterials: Multifunctional Materials for Biomedical Engineering," *ACS Nano* 7 (2013): 2891–2897, https://doi.org/10.1021/NN401196A.

19. Z. Xu, Z. Wu, P. Poulin, et al., "A state-of-the-Art Review on Carbon-based Nanomaterials for Engineering Applications," *Cleaner Materials* 19 (2026): 100363, https://doi.org/10.1016/J.CLEMA.2025.100363.

20. M. Ferda, *Biotribological behavior of polycaprolactone (PCL)/carbon quantum dots (CQDS) films* (Zenodo, 2024), https://doi.org/10.5281/ZENODO.12547548.

21. F. Mindivan and B. Boz, "A Scaffold Material: Reduced Graphene Oxide and Carbon Quantum Dots Filled Polycaprolactone Nanofibers," *Diamond and Related Materials* 153 (2025): 112039, https://doi.org/10.1016/J.DIAMOND.2025.112039.

22. F. Mindivan and M. Göktaş, "The Green Synthesis of Carbon Quantum Dots (CQDs) and Characterization of Polycaprolactone (PCL/CQDs) Films," *Colloids and Surfaces A: Physicochemical and Engineering Aspects* 677 (2023): 132446, https://doi.org/10.1016/J.COLSURFA.2023.132446.

23. K. Yazdani, "Green Graphene-Based Polymer Composites: a Pathway toward Sustainable Polymers," *Journal of Applied Materials Science* 1 (2025): 210140, https://doi.org/10.22034/JAMS.2025.210140.

24. V. U. Siddiqui, S. M. Sapuan, and M. R. Hassan, "Innovative Dispersion Techniques of Graphene Nanoplatelets (GNPs) through Mechanical Stirring and Ultrasonication: Impact on Morphological, Mechanical, and Thermal Properties of Epoxy Nanocomposites," *Defence Technology* 43 (2025): 13–25, https://doi.org/10.1016/J.DT.2024.04.018.

25. M. A. Azka, S. M. Sapuan, and E. S. Zainudin, "Enhancing Natural Fiber-Reinforced Biopolymer Composites with Graphene Nanoplatelets: Mechanical, Morphological, and Thermal Properties," *Nanotechnology Reviews* 14 (2025): 20250202, https://doi.org/10.1515/NTREV-2025-0202.

26. M. Hashemi, I. Ghasemi, A. Omrani, A. Rostami, C. J. Durán-Valle, and M. Qandalee, "Biodegradable Shape Memory Nanocomposites Based on PCL/PPC/Graphene: as a Proposal Material for Cardiovascular Stent," *Journal of Polymers and the Environment* 33 (2025): 2464–2479, https://doi.org/10.1007/S10924-025-03546-Z.

27. A. Raman, J. S. Jayan, V. D. Punetha, et al., "Exploring the Potential of Bioepoxy/Graphene Nanoplatelet Composites as Advanced Shape Memory Materials," *Materials Research Bulletin* 192 (2025): 113619, https://doi.org/10.1016/J.MATERRESBULL.2025.113619.

28. S. Ganeshkumar, H. A. Rahman, T. M. Gowtham, T. Adithya, I. Suyambulinagm, and J. Maniraj, "Multifunctional Polymer Composites: Design, Properties, and Emerging Applications—A Critical Review," *International Conference on Eco-friendly Fibers and Polymeric Materials* (Springer, 2024): 637–649, https://doi.org/10.1007/978-981-97-7071-7_45.

29. A. Navidfar and L. Trabzon, "Recent Advances in the Multifunctional Properties and Applications of Carbon Nanotube/Graphene Hybrid Polymer Nanocomposites," *Polymer Composites* 47 (2025): 29–51, https://doi.org/10.1002/PC.70159.

30. A. A. Musa, A. Bello, S. M. Adams, et al., "Nano-Enhanced Polymer Composite Materials: a Review of Current Advancements and Challenges," *Polymers* 17 (2025): 893, https://doi.org/10.3390/POLYM17070893.

31. R. Kandi, P. M. Pandey, M. Majood, and S. Mohanty, "Fabrication and Characterization of Customized Tubular Scaffolds for Tracheal Tissue Engineering by Using Solvent Based 3D Printing on Predefined Template," *Rapid Prototyping Journal* 27 (2021): 421–428, https://doi.org/10.1108/RPJ-08-2020-0186.

32. Q. Meng, S. Liu, Y. Yu, et al., "UV-Curable, Self-Healingand Rigid Polyurethane-UreaAcrylate Elastomers Reinforced with Zirconium Phosphate Nanosheets," *ACS Applied Polymer Materials* 8 (2026): 2815–2830, https://doi.org/10.1021/ACSAPM.5C04239.

33. M. Rostami, G. Jahed-khaniki, E. M. aghaee, et al., "Polycaprolactone/Polyacrylic Acid/Graphene Oxide Composite Nanofibers as a Highly Efficient Sorbent to Remove Lead Toxic Metal from Drinking Water and Apple Juice," *Scientific Reports* 14 (2024): 4372, https://doi.org/10.1038/S41598-024-54969-Y.

34. F. Dawaymeh, A. Agha, A. Alazzam, and M. Abd-Ellah, "Exploring Cyclic Olefin Copolymer (COC) for Flexible Silver Nanowire Electrode," *Scientific Reports* 14 (2024): 16989, https://doi.org/10.1038/s41598-024-68019-0.

35. S. Han, S. Pan, S. Li, et al., "Sustainable SiO_2@Montmorillonite Nanohybrid for High Mechanical Performance SLS-printed PA12 Nanocomposites," *Composites Communications* 65 (2026): 102848, https://doi.org/10.1016/J.COCO.2026.102848.

36. H. Zhou, Y. Xia, G. Mu, et al., "The Preparation and Characterization of Biodegradable PCL/PLA Shape Memory Blends," *Journal of Macromolecular Science, Part A* 58 (2021): 669–676, https://doi.org/10.1080/10601325.2021.1921598.

37. Y. Nashchekina, A. Chabina, A. Nashchekin, and N. Mikhailova, "Polycaprolactone Films Modified by L-Arginine for Mesenchymal Stem Cell Cultivation," *Polymers* 12 (2020): 1042, https://doi.org/10.3390/POLYM12051042.

38. Q. Meng, Q. Liu, S. Li, et al., "Interface-engineered PUA/Ag@HNT@ATMP Composites for Simultaneous Flame Retardancy, Mechanical Reinforcement, and Antibacterial Properties," *Chemical Engineering Journal* 524 (2025): 169416, https://doi.org/10.1016/J.CEJ.2025.169416.

39. S. Li, Y. Li, S. Han, et al., "Enhancing Fire Safety and Mechanical Properties of Polyurea Elastomer via Nitrogen-Boron Supramolecularly Modified Black Phosphorus," *Journal of Industrial and Engineering Chemistry* 159 (2026): 502–513, https://doi.org/10.1016/J.JIEC.2026.01.005.

40. L. Sun, T. X. Wang, H. M. Chen, et al., "A Brief Review of the Shape Memory Phenomena in Polymers and Their Typical Sensor Applications," *Polymers* 11 (2019): 1049, https://doi.org/10.3390/POLYM11061049.

41. S. K. Ghosh, S. S. Ganguly, S. Paul, T. Ghosh, A. K. Das, and N. C. Das, "Effect of Graphene Nanoplatelets and Nano Zinc Oxide on Gas Barrier and Antibacterial Properties of Thermoplastic Nanocomposites," *Polymer Engineering & Science* 64 (2024): 4181–4195, https://doi.org/10.1002/PEN.26840.

14392054, 2026, 3, Downloaded from https://onlinelibrary.wiley.com/doi/10.1002/mame.70360 by NICE, National Institute for Health and Care Excellence, Wiley Online Library on [08/11/2026]. See the Terms and Conditions (https://onlinelibrary.wiley.com/terms-and-conditions) on Wiley Online Library for rules of use; OA articles are governed by the applicable Creative Commons License

42. R. Martuci, S. J. Oliveira, M. Martuci, J. Reis-Campos, and M. H. Figueiral, "Antimicrobial Effect of Graphene in Dentistry: a Scoping Review," *Dentistry Journal* 13 (2025): 355, https://doi.org/10.3390/DJ13080355.

43. A. H. Hussein and Y. A. Yassir, "Graphene as a Promising Material in Orthodontics: a Review," *Journal of Orthodontic Science* 13 (2024): 24, https://doi.org/10.4103/JOS.JOS_3_24.

44. W. Han, Z. Wu, Y. Li, and Y. Wang, "Graphene family Nanomaterials (GFNs)—Promising Materials for Antimicrobial Coating and Film: a Review," *Chemical Engineering Journal* 358 (2019): 1022–1037, https://doi.org/10.1016/J.CEJ.2018.10.106.

45. H. Mohammed, A. Kumar, E. Bekyarova, et al., "Antimicrobial Mechanisms and Effectiveness of Graphene and Graphene-Functionalized Biomaterials. A Scope Review," *Frontiers in Bioengineering and Biotechnology* 8 (2020): 465, https://doi.org/10.3389/FBIOE.2020.00465.

14392054, 2026, 9, Downloaded from https://onlinelibrary.wiley.com/doi/10.1002/mame.70360 by NICE, National Institute for Health and Care Excellence, Wiley Online Library on [08/11/2026]. See the Terms and Conditions (https://onlinelibrary.wiley.com/terms-and-conditions) on Wiley Online Library for rules of use; OA articles are governed by the applicable Creative Commons License